A well-defined methodology to extract laminar flame speeds at engine-relevant conditions

Chaimae Bariki [*], Christian Schwenzer, Raik Hesse, Roman Glaznev, Heinz Pitsch, Joachim Beeckmann

Institute for Combustion Technology, RWTH Aachen University, 52056 Aachen, Germany

ARTICLE INFO

ABSTRACT

This paper presents a new method for accurate laminar flame speed measurements relevant to engine operating temperature and pressure conditions, where literature data are scarce or non-existent. The experimental setup consists of a high-pressure, high-temperature spherical chamber that combines optical and pressure-rise data collection techniques. The optical method is based on high-speed recordings of flame images using a schlieren setup, whereas the pressure-rise approach requires pressure measurements of isentropically compressed unburned gases taken during flame propagation. The range of usable data in the pressure-rise method is limited by stretch effects at lower pressures and the onset of instabilities at higher pressures. Here, the lower pressure limit was extended using optical data measured at isentropic conditions. A criterion to define the upper-pressure limit is proposed by the onset of instabilities during combustion that is especially useful for pressure readings taken in spherical chambers without optical access. Experimental laminar flame speeds are compared to those obtained with simulations using two detailed kinetic models, where very good agreement is found. Finally, a well-defined procedure is proposed showing how to obtain an extensive range of experimentally accurate laminar flame speed data that can be used to validate kinetic schemes by using only few measurements.

Novelty and Significance statement

The novelty of this paper is condensed in a clear and straightforward methodological approach to extracting high-fidelity data from a small number of experiments. While the optical and pressure-rise methods are not new, it is useful to know how to combine the two techniques and cross-validate them to ensure extracted data are accurate and free of effects such as instabilities. A new criterion is proposed to help detect the onset of instabilities regardless of their type. This can be valuable for research groups using only spherical chambers without optical access. A guideline is given at the end of the paper based on profound evidence for our claims using optical data. With the proposed methodology, accurate data can be obtained using only the pressure-rise method. Its application allows for obtaining engine-relevant data without replacing the bath gas with helium or argon.

1. Introduction

The laminar flame speed, $S_{L,u}$, is a fundamental physicochemical property of a combustible mixture characterizing its reactivity, exothermicity, and burning rate. Measuring laminar flame speeds is essential for the validation of kinetic mechanisms [1], engine design, and it serves as an input parameter in turbulent combustion models [2], e.g., the level-set combustion model [3,4]. A literature survey of nearly 200 papers published in major combustion journals on the experimental determination of $S_{L,u}$, conducted by Movaghar et al. [5], revealed that less than 8% of the measured data were performed at an initial pressure of $P > 10$ bar for C_1-C_4 n-alkanes flames. In contrast, more than 65%

were measured under atmospheric conditions. This drastic decrease in studies conducted at engine-relevant pressures relates to the experimental difficulties encountered at extreme thermodynamic conditions. It is therefore evident that laminar flame speeds are needed under these conditions, as they are scarce or non-existent. The main objective of the present study is addressing the methodology to extract high-fidelity laminar flame speeds at elevated temperatures and pressures.

Laminar flame speeds can be measured using Bunsen burners [6], heat flux burners [7], counterflow/stagnation burners [8], externally heated channels [9], shock tubes [10], or spherical chambers [11].

The first four configurations cannot provide data at engine-relevant conditions. The shock tube configuration was recently used by Ferris et al. [10] for the first time to measure $S_{L,u}$ of gaseous fuels at high temperature and atmospheric pressure. Using the same configuration, Susa et al. [12,13] measured laminar flame speeds of n-heptane and iso-octane flames. However, data are not reported at elevated pressures. Until today, the outwardly propagating spherical flame in a closed vessel is the only proven method to measure laminar flame speeds at conditions close to those found in internal combustion engines and gas turbines. More details related to each configuration can be found in the works of Egolfopoulos et al. [14], Faghih et al. [15], and Konnov et al. [16]. The conditions, as a function of pressure and temperature, achievable for each setup are summarized in Halter et al. [17] and Wang et al. [18]. The present study utilizes a spherical chamber.

In the spherical chamber configuration, after central ignition using an electrical spark or a laser in a quiescent homogeneous combustible mixture, a spherical flame is formed. It propagates outwardly until it reaches the chamber's wall. The laminar flame speed can be determined using two different approaches (more details can be found in Section 2.3):

1. Optical method: for this technique, images are recorded using high-speed schlieren, shadowgraphy, or laser tomography to obtain flame speeds. This method requires optical access to the chamber and is hereafter called the optical method.
2. Pressure-rise method: this technique requires recordings of the pressure trace during the combustion process. This approach is denoted here by the pressure-rise method.

Each approach has its advantages and disadvantages. Establishing a combined approach, where advantages are fostered and disadvantages are remedied, proves most valuable for flame speed evaluation of fuels under engine-relevant conditions. The optical method is suitable for investigating fuels not only at ambient conditions but also at elevated pressures and temperatures. Additionally, the optical method is useful for detecting cell development during flame propagation. On the other hand, this approach is time- and resource-consuming if a complete database has to be acquired. Additional limitations are related to the mechanical resistance of the chamber and the possibility of fuel decomposition during mixture preparation at high initial temperatures $T >$ 500 K [19]. There are also concerns about the usable radius data range for post-processing and which extrapolation technique should be used to obtain unstretched flame propagation speeds. A detailed discussion about these issues can be found in Chen et al. [20], Wu et al. [21], and Beeckmann et al. [22]. The pressure-rise approach is attractive because flame speeds can be obtained during the isentropic compression stage of a spherical flame propagation if the flame front is thin and smooth, and stretch, radiation, and buoyancy effects are negligible. This means that a single measurement covers a wide range of pressures and temperatures. In addition, it is possible to attain higher temperatures without the danger of fuel decomposition and prereactions because the mixture is prepared at a low temperature and only reaches high temperatures during compression phase. However, this method has been used less frequently over the years due to the assumptions invoked to derive laminar flame speeds and the associated large uncertainties. The useful pressure range that excludes data affected by stretch, confinement, and instabilities must be carefully monitored. Recent efforts were made by Movaghar et al. [5,23] and Halter et al. [17,24], who addressed the lower pressure limit that should be considered to avoid stretch effects for the conditions investigated. The lower pressure limit is apparatus-dependent, and no universal criterion has been defined to the authors' knowledge. For instance, a criterion of $P/P_0 > 2$ was defined based on experimental data [17,25], while $P/P_0 > 2.5$ has been suggested previously based on simulations [5,19]. For the higher pressure limit, however, no well-defined criterion exists to determine at which pressure the onset of instabilities occurs. This issue is not fully solved for the spherical chamber configurations without optical access,
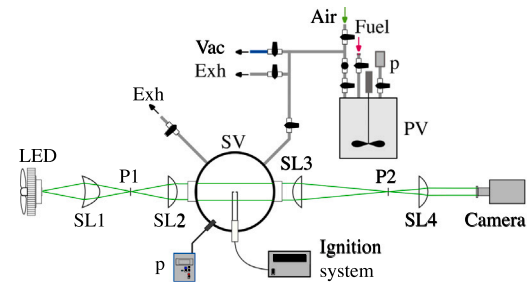

Fig. 1. Experimental setup. SL: spherical lens, P_x: pinhole, SV : spherical vessel, PV: premixing vessel, Vac: vacuum pump, Exh: exhaust, p: pressure sensor.

where flame imaging is not possible for detecting cell development and becomes a critical factor in those facilities.

Recently, we demonstrated that combining the optical and pressure-rise techniques provides high-fidelity data and reduces global uncertainties since they complement one another [26]. This combined method was employed in our recent work to obtain laminar flame speeds for slowly propagating flames [27]. Hinton et al. [28] showed that it is possible to obtain consistent values of the laminar flame speed using both methods when appropriate data processing is conducted. The present paper aims to push the analysis one step further by stressing the potential of combining both techniques to obtain consistent and meaningful data. Here, a novel criterion is proposed to identify the onset of instabilities based on pressure readings taken during the combustion process. Additionally, the previously established lower limit pressure is revisited to broaden the usable data range, enabling more accurate laminar flame speed determination. Experiments are reported at various initial pressures and temperatures, using methane and iso-octane as representative gaseous and liquid fuels. Air was used as an oxidizer.

2. Experimental approach

2.1. Apparatus and diagnostic configuration

Experiments were conducted in the Institute for Combustion Technology's high-pressure, high-temperature combustion chamber [26,29,30] at RWTH Aachen University. The setup's schematic is presented in Fig. 1. The internal shape of the combustion vessel is spherical with an inner diameter of 100 mm. Two quartz windows, each with a radius of 25 mm, were placed on opposing sides to allow for optical access. Flame propagation was imaged with a schlieren technique. A pulsed high-power LED emitting green light was combined with a high-speed CMOS camera (LaVision HighSpeedStar 6). The acquisition rate was set to 25 kHz with a field of view of 448×448 pixels^2 resulting in a magnification ratio of 11.41 px/mm. Optics include four spherical lenses and two pinholes with a diameter of 0.5 mm. During the combustion process, the pressure rise was monitored using a Kistler dynamic pressure transducer, with a full-scale value of 50 bar and a sampling rate of 25 kHz. The uncertainty of the pressure sensor at full-scale reading was ± 0.05 bar.

All fuel/air mixtures were prepared in a separate premixing vessel (1.35 l) using the partial pressure method [29]. Two temperature-compensated Keller pressure transducers, which covered the entire pressure range during mixture preparation, were used with different ranges of 3 and 30 bar to measure and control the filling process accurately. The 0–3 bar pressure transducer is used to fill in the small amount of gaseous or liquid fuel, while the 0–30 bar pressure transducer is used to fill in the air. Thus, mixture-preparation uncertainty was reduced by using pressure values close to the transducers' limits. Methane/air mixtures are prepared at a total pressure of 30 bar and

Table 1
Initial experimental conditions investigated and mixtures' properties.

Case	Fuel	Oxidizer	ϕ [–]	P_0 [bar]	T_0 [K]	Le_{eff} [–]
M1	Methane	Air	0.8	2.25	298	1.003
M2	Methane	Air	0.8	5.00	373	0.989
M3	Methane	Air	1.0	2.25	298	1.037
M4	Methane	Air	1.0	5.00	373	1.102
O1	Iso-octane	Air	0.9	2.50	373	2.206
O2	Iso-octane	Air	0.9	3.50	406	2.168
O3	Iso-octane	Air	0.9	5.00	448	2.132
O4	Iso-octane	Air	1.0	2.50	373	1.890
O5	Iso-octane	Air	1.0	3.50	406	1.863
O6	Iso-octane	Air	1.0	5.00	448	1.837
O7	Iso-octane	Air	1.1	2.50	373	1.608
O8	Iso-octane	Air	1.1	3.50	406	1.587

iso-octane/air mixtures are prepared at 20 bar to avoid fuel condensation. Liquid fuels were injected with a syringe into the premixing vessel, which was heated to vaporize the fuels, and the air was added subsequently. Mixtures in the premixing vessel were stirred using a rotating stirrer to ensure complete homogeneous mixing of fuel and air. One mixture was prepared to perform multiple measurements at one equivalence ratio, ensuring repeatability with exactly the same mixture. The combustion chamber and its periphery can be heated for measurements at elevated temperatures [29]. To ensure a clean combustion chamber prior to each filling, the chamber was first flushed with air, then with a combustible fuel/air mixture. After each flushing, the chamber was evacuated to 0.03 bar. The spherical chamber was subsequently filled with the targeted combustible mixture and was ignited at the chamber's center using a pair of electrodes of 1 mm diameter, which were arranged face to face. The electrode tip distance was set to 1.5 mm. The spark was generated using a two-step high-voltage system recently designed in-house [31]: the first output stage feeds an ignition coil, which generates a plasma between the electrode tips, and the second output stage generates a variable voltage of 500 to 2000 V DC, fed by the power capacitors. This output stage increases the energy of the already produced first-stage ignition plasma.

2.2. Selected conditions

Stoichiometric ($\phi = 1.0$) and lean ($\phi = 0.8$) methane/air flames were selected as validation cases for the proposed laminar flame speed extraction methodology. In addition, iso-octane was selected as a typical representative liquid fuel. It is rated with a Research Octane Number (RON) of 100. Together with n-heptane, it provides the basis for a primary reference fuel (PRF) relevant for gasoline engine development. Stoichiometric, lean ($\phi = 0.9$), and rich ($\phi = 1.1$) iso-octane/air flames were selected at various initial pressures and temperatures as listed in Table 1. It is worth stressing that initial pressures and temperatures were carefully calculated assuming an isentropic compression to compare the pressure-rise method's results with those measured for the isentropes using the optical method. The temperature of the unburned gas is determined from the pressure according to the isentropic-compression relationship ($T/T_0 = P/P_0^{1-1/\gamma_u}$, where γ_u is the specific heat capacity ratio of the unburned gas calculated at each initial condition based on thermodynamic data). Flame characteristics are calculated for a 1D unstretched laminar flame configuration using the open-source FlameMaster code [32]. The effective Lewis numbers are also added to Table 1. One can see that $Le_{\text{eff}} > 1$ for all investigated conditions except the lean methane case at high temperature and pressure (case M2), where $Le_{\text{eff}} = 0.989$. It can be deduced that only hydrodynamic instability evolves during flame propagation. The definition of Le_{eff} is given in the Supplemental Material. Two published kinetic mechanisms are chosen to compare the experimental data to: (1) the chemical mechanism of ITV updated by Langer et al. [33], which was extensively validated for a large number of fuels, and (2) the C3 mechanism by the Computational Chemistry Consortium published by Dong et al. [34], which has been validated with a large number of fuels and conditions.

2.3. Laminar flame speed evaluation

As mentioned above, two approaches to measuring laminar flame speeds are considered in this study: the optical method and the pressure-rise method. Each approach is presented here in detail.

2.3.1. Optical method

At the early stage of outwardly propagating flames in a spherical combustion vessel, the pressure-rise is negligible, and the flame radius, R_{f}, can be determined based on the recorded schlieren images. The flame speed with respect to the burned gas can be calculated as $S_{\text{L},b} = dR_{\text{f}}/dt$ based on the assumption that the burned gas is at rest. For spherically expanding flames, the stretch rate is defined as the temporal change of a flame surface element $K = (2/R_{\text{f}})(dR_{\text{f}}/dt)$. To extrapolate to zero stretch, the linear scheme by Matalon et al. [35], defined as

$$S_{\text{L},b}^0 - S_{\text{L},b} = \mathcal{L}_b K, \tag{1}$$

and the nonlinear method by Kelley et al. [36]

$$S_{\text{L},b}^0 t + c = R_{\text{f}} + 2\mathcal{L}_b \ln R_{\text{f}} - 4\frac{\mathcal{L}_b^2}{R_{\text{f}}} - \frac{8}{3}\frac{\mathcal{L}_b^3}{R_{\text{f}}^2} \tag{2}$$

were used, where c is an integration constant and the parameter $\mathcal{L}_b$ is the burned-gas Markstein length, which represents the sensitivity of flame speed to stretch. After extrapolating to zero stretch, the laminar flame speed is determined from mass continuity through a planar unstretched flame, $S_{\text{L},u}^0 = \rho_b/\rho_u \cdot S_{\text{L},b}^0$, where ρ_b and ρ_u represent the densities of the burned and the unburned gas.

2.3.2. Pressure-rise method

The laminar flame speed $S_{\text{L},u}$ can be calculated on the basis of the pressure time history $P(t)$ recorded during the combustion process. This approach called the pressure-rise method, is based on the following assumptions: infinitely thin smooth spherical flame front, spatially uniform pressure during combustion, isentropic compression of unburned gases, both burned and unburned gases are ideal, and radiation and buoyancy effects are negligible. The following expression has been derived by Fiock and Marvin [37]

$$S_{\text{L},u} = \frac{dR_{\text{f}}}{dt} - \frac{(R_{\text{w}}^3 - R_{\text{f}}^3)}{3\gamma_u R_{\text{f}}^2 P}\frac{dP}{dt}, \tag{3}$$

where R_{w} corresponds to the inner wall chamber radius. The burned mass fraction is defined as $x = m_b/m_0$, where $m_0 = m_u + m_b$ according to mass conservation. Therefore, the unburned mass can be written as $m_u = (1 - x) \cdot m_0$, yielding

$$\frac{4\pi}{3}\left(R_{\text{w}}^3 - R_{\text{f}}^3\right)\rho_u = (1 - x)\frac{4\pi}{3}R_{\text{w}}^3\rho_0. \tag{4}$$

Since the unburned gas is compressed isentropically, $\rho_0/\rho_u = (P_0/P)^{1/\gamma_u}$, one can deduce the following relationship between the flame radius and the pressure trace

$$\frac{R_{\text{f}}}{R_{\text{w}}} = \left[1 - (1 - x)\left(\frac{P_0}{P}\right)^{1/\gamma_u}\right]^{1/3}. \tag{5}$$

Substituting Eq. (5) into Eq. (3) yields

$$S_{\text{L},u} = \frac{R_{\text{w}}}{3}\left[1 - (1 - x)\left(\frac{P_0}{P}\right)^{1/\gamma_u}\right]^{-2/3}\left(\frac{P_0}{P}\right)^{1/\gamma_u}\frac{dx}{dt}. \tag{6}$$

In the present paper, the burned mass fraction and laminar flame speed are calculated on the basis of the pressure signal with a publicly available data reduction tool provided by the National Institute for Standards and Technology (NIST) [38], which provides both 2-zone model by Metghalchi and Keck [39] and a multi-zone model by Elia et al. [40]. To provide most accurate data, the multi-zone model is used to extract the laminar flame speed from the pressure signal in this work.

A comparison between the two-zone and multi-zone model is given in the supplemental material for completeness.

Prior to using the tool, all pressure data are smoothed by applying a moving average with a sliding window of 35 data points. The window size was carefully chosen so that characteristics such as slope and inflection points are not modified. This step was required to prevent amplification of background noise on the derivatives of the pressure sensor data.

The NIST tool offers the option to apply an optically thin model (OTM) to correct for decelerating radiation heat loss. Here, we chose not to apply this radiation model for two reasons: (1) flames investigated in this work are mostly fast-burning, and radiation effects are expected to be small or negligible [23,41], and (2) the optically thin model exclusively addresses radiation emission, disregarding absorption. Therefore, when correcting data with the optically thin model, the resulting flame speed is biased towards higher values. Based on the points mentioned above, laminar flame speeds are evaluated assuming adiabatic conditions. The supplemental material compares corrected and uncorrected radiation data for completeness. It is important to highlight that the onset of instability has a bigger effect on $S_{L,u}$ in the examined flames than radiation heat loss.

2.3.3. Uncertainty quantification

In order to provide high-fidelity data for kinetic mechanism validation, accurate quantification of uncertainties arising from experimental measurements is crucial. Here, the same uncertainty analysis has been used by Bariki et al. [26] is utilized. The combined uncertainty in laminar flame speed resulting from mixture preparation, initial temperatures, and pressures together with data post-processing, was calculated using the residual sum of squares method. Note that at least four measurements for each condition were performed to ensure repeatability of experiments. An uncertainty between 2 to 5% was obtained based on a 95% confidence interval. Unless otherwise stated, the uncertainties are presented by vertical error bars for the optical measurements.

3. Results

3.1. Flame morphology and propagation speed

Fig. 2 represents a sequence of typical schlieren images of iso-octane/air flames at $\phi = 0.9$ at different initial temperatures and pressures (O1 & O3). For the present study, only images corresponding to a flame front radius greater than at least 8 mm were used to avoid ignition effects (cf. Fig. 2a and α). A criterion of a pressure increase of 1% was imposed to determine the last image that should be used to derive the flame speed with the optical method (cf. Fig. 2c and γ). To determine the flame radius from the raw images recorded by the high-speed camera, the surface of the spherical flame is projected, and the instantaneous flame front radius is deduced. The cracks seen in Fig. 2α-γ, at $P_0 = 5.0$ bar and $T_0 = 448$ K, are artifacts due to ignition and not related to cellular development. Cell development and splitting into smaller cells can be observed at a later stage, as illustrated for instance in Fig. 2δ-ϵ.

Fig. 3 depicts the evolution of the propagation speed $S_{L,b}$ as a function of the stretch rate K for the same flames (O1 & O3). As seen in Fig. 3, there is a marginal difference between the extrapolated values using linear and nonlinear techniques. Unless otherwise specified, the non-linear extrapolation by Kelley et al. [36] is used in the present work. Recall that an increase in pressure decreases stretch response, while increased temperature yields the opposite. However, the pressure effect dominates along an isentropic compression. The burned-gas Markstein length $\mathcal{L}_b$ approaches zero with increasing P_0 and T_0, indicating that stretch effects on flame speed decrease at high initial pressure and temperature conditions. Consequently, the known lower pressure limits defined in the literature can even be relaxed, and the usable data range can be extended as shown in Section 3.3.

3.2. Onset of instabilities

The pressure range where instabilities evolve should also be excluded from the flame speed evaluation. Omari and Tartakovsky [42] showed that a rapid increase in the laminar flame speed occurs for some mixtures, which can be linked to the onset of instabilities. However, no pictures were provided so far for detailed analysis and to support the hypothesis. When potential instabilities occur at a later stage of the combustion process, a clear identification of this rapid increase could be helpful to exclude data when cellularities are developing. However, it will be very challenging to identify the onset of instabilities when the flame is unstable all along from the beginning. Consequently, an overestimation of the derived flame speeds, only using the pressure method, cannot be avoided for spherical chambers without optical access. In the present study, we propose a viable alternative to determine the onset of instabilities avoiding any upcoming ambiguities. This can be done by analyzing the dependence of the relative pressure-rise rate K_p of the pressure trace, which is defined as

$$K_p = \frac{1}{P}\frac{\mathrm{d}P}{\mathrm{d}t}. \tag{7}$$

Inflection points can be detected coinciding with the onset of instabilities. Notably, very high pressures and temperatures could be achieved within a few milliseconds during the isentropic compression. This duration is sufficiently short enough to prevent fuel decomposition prior to combustion. Therefore, an abrupt change in K_p is only linked to flame wrinkling. The absence of inflection points in K_p often means the flame propagates without any cell development. However, K_p inflection points can also be absent when a flame is unstable during the entire combustion process. Note that the flames investigated in this paper only sustained hydrodynamic instability at elevated pressures and temperatures. Therefore, the flames are stable before and unstable after the identified inflection points, respectively. The inflection points characteristics such as the density ratio (ρ_b/ρ_u) and the flame thickness ($l_f = \lambda/(\rho_u c_p S_{L,u})$) are given in Table S1 of the supplemental material. The Peclet number, defined as the flame radius divided by the flame thickness (Pe $= R_f/l_f$), is also a relevant parameter since it represents the ratio of convective to thermodiffusive effects depending on the gas thermal expansion and the Lewis number. The critical Peclet number guides an understanding of flame instabilities's initiation.

It is important to highlight that the effect of unsteady pressure-rise on the laminar flame speed measured using the pressure-rise method has been investigated numerically by Wang et al. [43] through the evaluation of K_p. It was found that the latter has a marginal effect on the reaction zone and, therefore, on the flame speed. A notable impact is found to be at very high pressures and temperatures, which is not the case for the conditions investigated in the present work. The same effect has been addressed by Jayachandran and Egolfopoulos [44] using the pressure rise number defined as PRN= $t_f^0 K_p$, where t_f^0 is a characteristic time scale of flame propagation.

Fig. 4 depicts the evolution of K_p calculated using Eq. (7) based on stoichiometric methane experiments over the normalized pressure for two different initial pressures and temperatures (cases M3 & M4). At $P_0 = 5$ bar & $T_0 = 373$ K, an inflection point can be easily identified at approximately $P/P_0 = 2$. This corresponds to the onset of instabilities because the pressure increase accelerates quickly. This is further confirmed by analyzing the schlieren images recorded during flame propagation. Two exemplary schlieren images were added to Fig. 4 corresponding to flames at $P/P_0 = 2$: one in a blue frame for case M4 and the other one in a red frame for case M3. One can see that the flame exhibits cellular instabilities for case M4 at $P/P_0 = 2$, unlike case M3, where the flame front exhibits minor disturbances that are linked to ignition effects. Therefore, the flame becomes unstable after the identified turning point, which can be considered a criterion for detecting instability development.

Although, in our case, the optically accessible window range has a radius of only 2.5 cm, and the flame radius cannot be extracted based
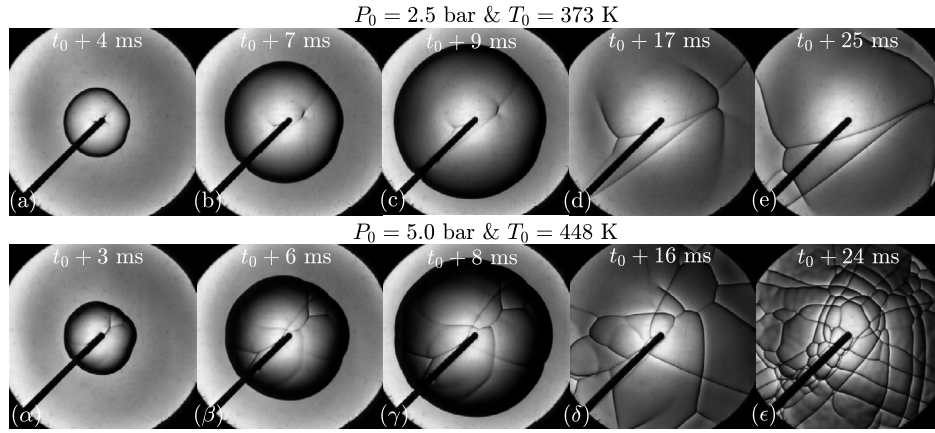
Fig. 2. Sequence of typical schlieren images of iso-octane/air mixtures at $\phi = 0.9$. First row: $P_0 = 2.5$ bar and $T_0 = 373$ K (O1); second row: $P_0 = 5.0$ bar and $T_0 = 448$ K (O3).
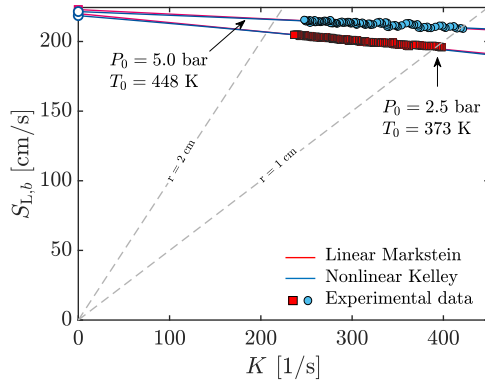

Fig. 3. The burned-gas flame speed as a function of the stretch rate of iso-octane/air mixtures at $\phi = 0.9$ for initial conditions $P_0 = 2.5$ bar and $T_0 = 373$ K (O1), $P_0 = 5.0$ bar and $T_0 = 448$ K (O3).

Fig. 4. Relative pressure-rise rate as a function of the normalized pressure of stoichiometric methane/air flames at various initial pressures and temperatures (cases M3 & M4). The inserted red and blue framed images correspond to the flame schlieren images at the inflection point $P/P_0 = 2$ for cases M3 and M4, respectively. (For interpretation of the references to color in this figure legend, the reader is referred to the web version of this article.)

on the images when it grows larger than the window's size, the flames' morphology can still be analyzed to identify at which pressure flames become unstable. This information is invaluable for providing accurate flame speed data. Note that at $P/P_0 = 3$, heat losses gain importance in case M3, corresponding to a flame radius of 4.5 cm. For case M4, this point is irrelevant since instabilities are already occurring, and the data are unusable above $P/P_0 = 2$.

A similar analysis has been conducted for iso-octane flames. The relative pressure-rise vs. pressure is shown in Fig. 5. At $P_0 = 5$ bar & $T_0 = 448$ K (blue lines), a rapid increase is identified at approximately $P/P_0 = 2.6$ and $P/P_0 = 1.68$ for $\phi = 0.9$ and $\phi = 1.0$, respectively. For the lean iso-octane flame, cellular structures were identified based on schlieren images at higher initial pressure and temperature as shown in Fig. 2δ-ϵ. This means that the rapid increase, highlighted by a circle in Fig. 5, is linked to the onset of instabilities. This also applies to the stoichiometric case where instabilities occur earlier as the initial pressure and temperature increase (cf. cases O5 vs. O6). By further increasing the equivalence ratio to $\phi = 1.1$, instabilities appear at $P/P_0 = 1.6$ for case O8 (cf. orange lines). Note that the condition at $P_0 = 5$ bar & $T_0 = 448$ K is not included for a rich mixture because the flame is unstable right from the beginning due to the increasing influence of thermodiffusive driven instabilities.

It can be inferred that, even without optical access, the K_p criterion is well suited to identify the onset of instabilities, as illustrated in Figs. 4 and 5. The rapid increase in K_p coincides with flame cell splitting, and schlieren images are given to support this finding. It is noteworthy that in some cases without optical access, flames can be unstable from the very beginning. Hence, the comparison of K_p for
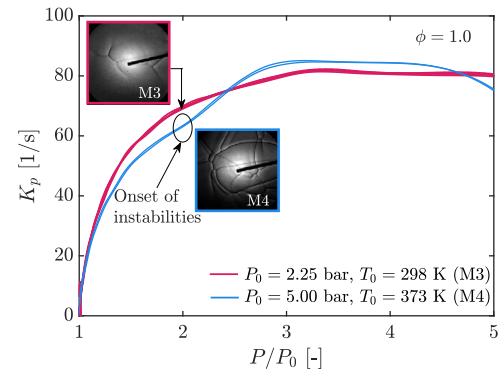
different conditions will not yield information on the onset of instabilities, and no distinction can be made if data are stable or unstable. In those cases, it is suggested to conduct an additional experiment on the isentrope at lower pressure and temperature to identify if the flame becomes unstable. Lastly, it is important to highlight that autoignition can also compromise the pressure method data and make it unsuitable for laminar flame speed extraction. However, this can be easily identified based only on pressure traces. As shown by Lawson et al. [45], pressure exhibits oscillations when end-gas autoignition occurs. A rapid rise in the fractional rate of pressure change is obtained. Consequently, this effect will also be captured in the K_p plot, making K_p a suitable parameter to track and select data unaffected by the compromising processes developed during the flame propagation. The K_p criterion would be successful without identifying the correct source of the inaccuracy.

3.3. Laminar flame speeds

Fig. 6 shows laminar flame speeds as a function of pressure and the corresponding unburned temperature of a lean and a stoichiometric methane flame. For each equivalence ratio, two initial pressures and temperatures were investigated, and the results were evaluated using optical and pressure-rise techniques. Recall that the condition at $P_0 = 5.0$ bar and $T_0 = 373$ K was calculated assuming isentropic compression and to compare the results with each other, obtained using the optical and the pressure-rise method. As can be seen in Fig. 6, good
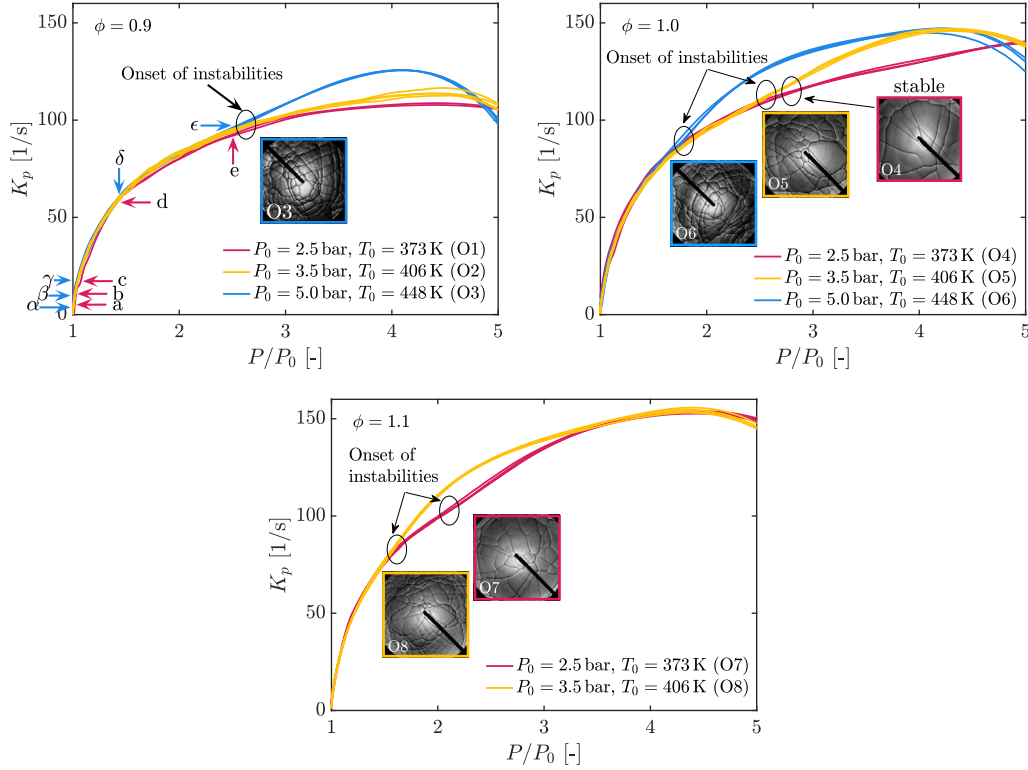
Fig. 5. Relative pressure-rise rate as a function of the normalized pressure for iso-octane/air flames at three equivalence ratios and various initial pressures and unburned temperatures (cases O1, O2, O3, O4, O5, O6, O7 & O8). (For interpretation of the references to colour in this figure legend, the reader is referred to the web version of this article.)
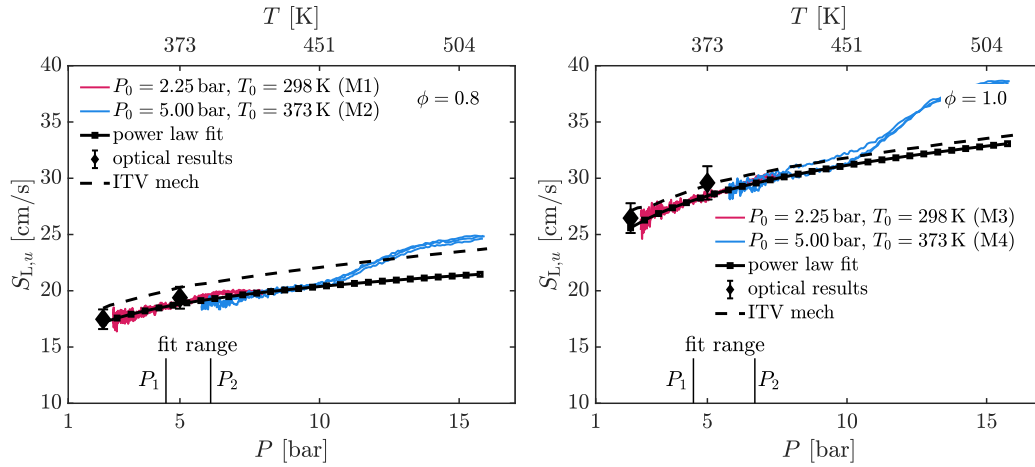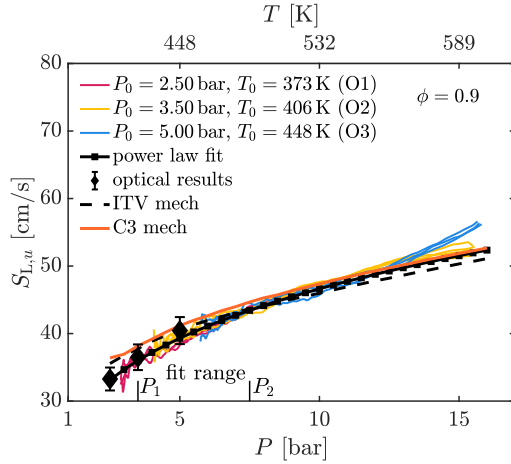

Fig. 6. Laminar flame speeds of methane/air as a function of pressure and unburned temperature at $\phi = 0.8$ and 1.0 (cases M1, M2, M3, and M4). Lines and hollow symbols correspond to pressure-rise and optical results, respectively. Overlaid dashed curves are obtained using the ITV mechanism by Langer et al. [33]. (For interpretation of the references to color in this figure legend, the reader is referred to the web version of this article.)

agreement is achieved when comparing the single hollow symbols and lines obtained using optical and pressure-rise data, which demonstrates the validity of the assumptions made for the pressure-rise method. The ITV mechanism [33] predicts the experimental results at $\phi = 1.0$, and over-predicts the results by less than 10% for the lean case. Moreover, the onset of instabilities can be identified as a rapid increase in laminar flame speed in Fig. 6 confirming the prediction from the inflection point in K_p. Consequently, the flame speeds shown in Fig. 6 at $P > 10$ bar should not be used for kinetic model validation.

According to the literature, data could be extracted for the methane case with high initial pressure and temperature (M4) from twice the

initial pressure onwards ensuring the absence of stretch effects on the laminar flame speed. Since the experiment was performed at 5 bar, accordingly, valid flame speeds could be extracted for $P > 10$ bar. However, the onset of instabilities is at the same pressure, and all data would be useless. By performing another experiment on the same isentrope (M3), it can be seen that the unstretched flame speeds from the lower and higher pressure case overlap at $P \geq 6.5$ bar (cf. red line in Fig. 6 bottom). Therefore, data from case M4 with an initial pressure of 5 bar is usable from 6.5 to 10 bar, drastically increasing its valid flame speed range. In fact, the advantage of conducting this type of experiment, using two conditions where one corresponds to the

Fig. 7. Laminar flame speeds of lean iso-octane/air ($\phi = 0.9$) flames as a function of pressure and unburned temperature at initial conditions of $T_0 = 373$ K & $P_0 = 2.5$ bar, $T_0 = 406$ K & $P_0 = 3.5$ bar, and $T_0 = 448$ K & $P_0 = 5.0$ bar (cases O1, O2 & O3). (For interpretation of the references to color in this figure legend, the reader is referred to the web version of this article.)

Fig. 8. Laminar flame speeds of stoichiometric iso-octane/air ($\phi = 1.0$) flames as a function of pressure and unburned temperature at initial conditions of $T_0 = 373$ K & $P_0 = 2.5$ bar, $T_0 = 406$ K & $P_0 = 3.5$ bar, and $T_0 = 448$ K & $P_0 = 5.0$ bar (cases O4, O5 & O6). (For interpretation of the references to color in this figure legend, the reader is referred to the web version of this article.)

isentropic compression of the other, is that a wide data range can be obtained using only two measurements.
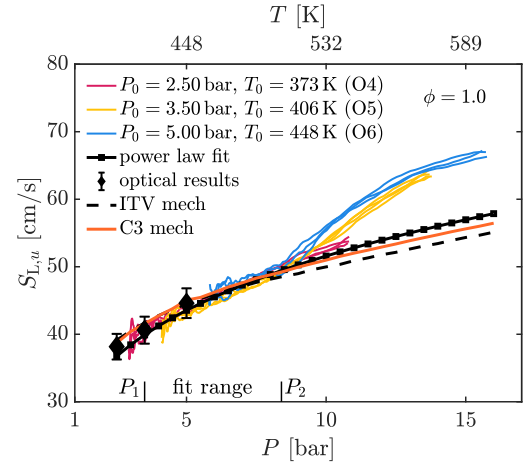
Similar conclusions are drawn for lean iso-octane/air flames ($\phi = 0.9$) as shown in Fig. 7: good agreement between the flame speeds derived using the optical and the pressure-rise technique is obtained. The kinetic model by Langer et al. [33] predicts the experimental results very well. Here, additional simulations were performed using the C3 mechanism [34]. It can be seen that the predicted flame speed using the latter mechanism also follows the experimental results closely. The C3 mechanism is performing slightly better at elevated pressures and temperatures. However, the difference is within the uncertainty of the experiment.

While for the methane cases, it was found that the valid range of a high-pressure, high-temperature case (M4) can be increased by over-lapping pressure-rise results, another extension of the lower pressure limit was found by applying a similar methodology to the iso-octane experiments. A measurement is performed with 1.4 times the initial pressure of the first measurement. In that way, the optical result of cases O2, O5, and O8 with an initial pressure of 3.5 bar and an initial temperature of 406 K (cf. black symbols in Figs. 7–9) can be used as a reference point for the pressure-rise results of the 2.5 bar cases. Recall that laminar flame speeds from the optical method are extrapolated to zero stretch using Eq. (2). Therefore, when the laminar flame speed obtained in the pressure-rise method intersects this point, it is likewise unaffected by stretch effects (cf. red line in Figs. 7–9). This is the case for equivalence ratios 0.9, 1.0, and 1.1, where the optical results of the 3.5 bar & 406 K case lie directly on the pressure-rise data of the respective 2.5 bar & 373 K case. Moreover, one can see that the pressure-rise data of cases O4 and O5 overlap over a wide region in Fig. 8. Valid flame speed data are then obtained from 3.5 bar until the onset of instabilities.

The mixture-dependent onset of instabilities derived from the inflection point of K_p marks the upper limit of valid flame speed data. At equivalence ratios of $\phi = 1.0$ and 1.1, the onset of instabilities occurs earlier than at $\phi = 0.9$ because of thermodiffusive effects (cf. Figs. 8 and 9). It is important to emphasize that the pressure–temperature condition of $P_0 = 5.0$ bar and $T_0 = 448$ K at $\phi = 1.1$ was excluded because the flame becomes unstable shortly after ignition.

3.3.1. Flame speed correlation

A power-law correlation for the dependence of temperature and pressure is commonly used to fit laminar flame speeds, which can be
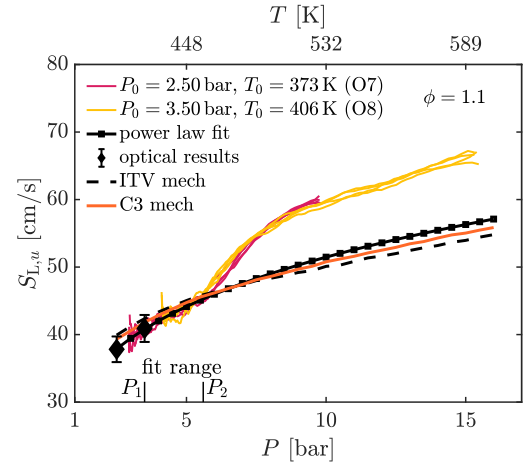
Fig. 9. Laminar flame speeds of rich iso-octane/air ($\phi = 1.1$) flames as a function of pressure and unburned temperature at initial conditions of $T_0 = 373$ K & $P_0 = 2.5$ bar and $T_0 = 406$ K & $P_0 = 3.5$ bar (cases O7 & O8). (For interpretation of the references to color in this figure legend, the reader is referred to the web version of this article.)

Table 2
Power-law fit results for Eq. (8).

Fuel	ϕ [–]	$S_{L,u,ref}$ [cm/s]	T_{ref} [K]	P_{ref} [bar]	P_1 [bar]	P_2 [bar]	α [–]	γ [–]
Methane	0.8	17.18	298	2.25	4.5	6.1	0.115	1.382
Methane	1.0	25.59	298	2.25	4.5	6.7	0.132	1.391
Iso-octane	0.9	33.14	373	2.5	3.5	7.5	0.246	1.345
Iso-octane	1.0	36.76	373	2.5	3.5	8.4	0.244	1.327
Iso-octane	1.1	37.88	373	2.5	3.5	5.6	0.221	1.328

written as

$$S_{L,u} = S_{L,u,ref} \left(\frac{P}{P_{ref}} \right)^\alpha, \quad \text{where} \quad T = T_{ref} \left(\frac{P}{P_{ref}} \right)^{\frac{\gamma-1}{\gamma}}, \tag{8}$$

where $S_{L,u,ref}$ is the laminar flame speed at a reference condition P_{ref} and T_{ref}, and the exponent α depends on the mixture composition. Table 2 includes all calculated power-law fit parameters and the corresponding pressure range (P_1 to P_2) used in the fitting process. These parameters were deduced individually for the five investigated mixtures. The effect of changing the equivalence ratio is therefore

implicitly taken into account in Eq. (8) through α and γ parameters. The obtained results are added to Figs. 6–9 (cf. black line with filled symbols). The methane case at $P_0 = 2.25$ bar, $T_0 = 298$ K and $\phi = 0.8$ (M1) does not develop instabilities before the flame reaches the wall. Therefore, the upper limit P_2 is chosen before the effect of wall heat loss at $P_2 = 6.1$ bar, which is below the inflection point of case M2 at $P = 10.5$ bar. The same approach applies to case M3, where the wall effects begin at $P_2 = 6.7$ bar and to case O1 at $P_2 = 7.5$ bar, respectively. In these three cases, the power-law is fitted with an upper-pressure limit below the onset of instabilities identified with K_p. Figs. 6 and 7 show that the use of the power-law beyond P_2 still overlaps with the extracted flame speed data that are free of instabilities. The power-law relationship can therefore represent the experimental data up to the onset of instabilities at 10.5 bar (M1 & M2), 10 bar (M3 & M4), and 13 bar (O1–O3). For iso-octane cases O4–O6 ($\phi = 1.0$), the inflection point was identified at $P_2/P_0 = 1.68$, which corresponds to a maximum pressure of $P_2 = 8.4$ bar. The K_p inflection point in cases O7 and O8 appears at $P_2/P_0 = 1.6$ which corresponds to $P_2 = 5.6$ bar.

When the power-law is applied at 2.5 bar, it matches the unstretched flame speed of the optical method in all investigated cases. This further validates the applicability of the power-law. The relationship can also be used to predict flame speeds beyond the instability limit, where the experiment cannot provide stable flame speed data.

4. Concluding remarks

The optical and pressure-rise methods for extracting laminar flame speeds are addressed in this paper. The potential of combining both techniques to significantly extend the range of valid experimental data is highlighted. Experimental measurements were conducted using the RWTH high-pressure, high-temperature spherical combustion chamber. Additionally, 1D unstretched premixed flame simulations were performed using two different published kinetic mechanisms. The outcomes of the present study can be summarized as follows:

- A new criterion is proposed based on the pressure trace to define the onset of the instability limit, which can be a crucial factor for pressure traces recorded in spherical chambers without optical access.
- Measuring conditions on a single isentrope enables to cross-validate data obtained by the optical and pressure-rise methods. Additionally, optical method flame speed results can be used to classify overlapping pressure-rise flame speeds to be unaffected by stretch. Hence, the lower pressure limit for the pressure-rise method can be relaxed in many cases and might have to be increased in some cases, where stretch effects play a major role at higher pressure.
- Comparison of experiment and 1D simulation shows that the ITV mechanism can predict the isentropic increase of methane flame speeds well, even at elevated pressure and temperature. For iso-octane, the C3 mechanism and the ITV mechanism predict the flame speed evolution very well.

In conclusion, the study shows how to obtain a large range of experimentally validated laminar flame speeds that can be used for kinetic mechanisms validation. As a result, the following procedure is recommended to obtain a large range of engine-relevant experimental flame speeds:

1. Perform an experiment with initial conditions of your choice.
2. Conduct an experiment with the same mixture composition and approximately 1.4–1.5 times the initial pressure. The initial temperature is determined by the isentropic compression relationship.

3. After post-processing the optical and pressure data, check if the optical method's flame speed result of the higher pressure experiment coincides with the pressure-rise method's flame speed result of the lower pressure case. If so, this pressure P_1 marks the lower limit of the power-law fit. Otherwise, use twice the initial pressure as the lower limit as recommended elsewhere in the literature.
4. Plot the relative pressure change K_p over the relative pressure P/P_0 and identify the inflection point corresponding to the onset of instabilities. This pressure P_2 marks the upper limit of the power-law fit.
5. Perform a power-law fit with laminar flame speed data extracted from the pressure-rise data between the minimum and maximum pressure. The result is a curve with experimental flame speeds that can be extrapolated to the lowest investigated pressure as well as to high-pressure, high-temperature conditions.

CRediT authorship contribution statement

Chaimae Bariki: Writing – review & editing, Writing – original draft, Visualization, Validation, Methodology, Investigation, Formal analysis, Data curation, Conceptualization. **Christian Schwenzer:** Writing – review & editing, Visualization, Validation, Investigation, Formal analysis, Data curation. **Raik Hesse:** Writing – review & editing, Validation, Formal analysis. **Roman Glaznev:** Writing – review & editing, Validation, Formal analysis. **Heinz Pitsch:** Writing – review & editing, Validation, Formal analysis. **Joachim Beeckmann:** Writing – review & editing, Validation, Supervision, Methodology, Funding acquisition, Formal analysis, Conceptualization.

Declaration of competing interest

The authors declare that they have no known competing financial interests or personal relationships that could have appeared to influence the work reported in this paper.

Acknowledgment

Appendix A. Supplementary data

Supplementary material related to this article can be found online at https://doi.org/10.1016/j.combustflame.2024.113612.

References

[1] A. Holley, X. You, E. Dames, H. Wang, F.N. Egolfopoulos, Sensitivity of propagation and extinction of large hydrocarbon flames to fuel diffusion, Proc. Combust. Inst. 32 (1) (2009) 1157–1163.

[2] T. Poinsot, Prediction and control of combustion instabilities in real engines, Proc. Combust. Inst. 36 (1) (2017) 1–28.

[3] N. Peters, Turbulent Combustion, Cambridge University Press, 2000, URL https://doi.org/10.1017/CBO9780511612701.

[4] H. Pitsch, A consistent level set formulation for large-eddy simulation of premixed turbulent combustion, Combust. Flame 143 (4) (2005) 587–598.

[5] A. Movaghar, R. Lawson, F.N. Egolfopoulos, Confined spherically expanding flame method for measuring laminar flame speeds: Revisiting the assumptions and application to C_1–C_4 hydrocarbon flames, Combust. Flame 212 (2020) 79–92.

[6] T. Echekki, M. Mungal, Flame speed measurements at the tip of a slot burner: Effects of flame curvature and hydrodynamic stretch, Symp. (Int.) Combust. 23 (1) (1991) 455–461.

[7] L. De Goey, A. Van Maaren, R. Quax, Stabilization of adiabatic premixed laminar flames on a flat flame burner, Combust. Sci. Tech. 92 (1–3) (1993) 201–207.

[8] C. Ji, E. Dames, Y.L. Wang, H. Wang, F.N. Egolfopoulos, Propagation and extinction of premixed C_5–C_{12} n-alkane flames, Combust. Flame 157 (2) (2010) 277–287.

[9] M. Akram, S. Kumar, Experimental studies on dynamics of methane–air premixed flame in meso-scale diverging channels, Combust. Flame 158 (5) (2011) 915–924.

[10] A.M. Ferris, A.J. Susa, D.F. Davidson, R.K. Hanson, High-temperature laminar flame speed measurements in a shock tube, Combust. Flame 205 (2019) 241–252.

[11] B. Lewis, G. Von Elbe, Determination of the speed of flames and the temperature distribution in a spherical bomb from time-pressure explosion records, J. Chem. Phys. 2 (5) (1934) 283–290.

[12] A.J. Susa, A.M. Ferris, D.F. Davidson, R.K. Hanson, Experimental shock tube measurements of laminar burning velocity of n-heptane and iso-octane in the negative temperature coefficient regime, in: AIAA Scitech 2019 Forum, 2019, p. 0460.

[13] A.J. Susa, A.M. Ferris, D.F. Davidson, R.K. Hanson, Experimental observation of negative temperature dependence in iso-octane burning velocities, AIAA J. 57 (10) (2019) 4476–4481.

[14] F.N. Egolfopoulos, N. Hansen, Y. Ju, K. Kohse-Höinghaus, C.K. Law, F. Qi, Advances and challenges in laminar flame experiments and implications for combustion chemistry, Prog. Energy Combust. Sci. 43 (2014) 36–67.

[15] M. Faghih, Z. Chen, The constant-volume propagating spherical flame method for laminar flame speed measurement, Sci. Bull. 61 (16) (2016) 1296–1310.

[16] A.A. Konnov, A. Mohammad, V.R. Kishore, N.I. Kim, C. Prathap, S. Kumar, A comprehensive review of measurements and data analysis of laminar burning velocities for various fuel+ air mixtures, Prog. Energy Combust. Sci. 68 (2018) 197–267.

[17] F. Halter, Z. Chen, G. Dayma, C. Bariki, Y. Wang, P. Dagaut, C. Chauveau, Development of an optically accessible apparatus to characterize the evolution of spherically expanding flames under constant volume conditions, Combust. Flame 212 (2020) 165–176.

[18] Y. Wang, A. Movaghar, Z. Wang, Z. Liu, W. Sun, F.N. Egolfopoulos, Z. Chen, Laminar flame speeds of methane/air mixtures at engine conditions: Performance of different kinetic models and power-law correlations, Combust. Flame 218 (2020) 101–108.

[19] C. Xiouris, T. Ye, J. Jayachandran, F.N. Egolfopoulos, Laminar flame speeds under engine-relevant conditions: uncertainty quantification and minimization in spherically expanding flame experiments, Combust. Flame 163 (2016) 270–283.

[20] Z. Chen, M.P. Burke, Y. Ju, Effects of compression and stretch on the determination of laminar flame speeds using propagating spherical flames, Combust. Theor. Model. 13 (2) (2009) 343–364.

[21] F. Wu, W. Liang, Z. Chen, Y. Ju, C.K. Law, Uncertainty in stretch extrapolation of laminar flame speed from expanding spherical flames, Proc. Combust. Inst. 35 (1) (2015) 663–670.

[22] J. Beeckmann, R. Hesse, J. Schaback, H. Pitsch, E. Varea, N. Chaumeix, Flame propagation speed and markstein length of spherically expanding flames: Assessment of extrapolation and measurement techniques, Proc. Combust. Inst. 37 (2) (2019) 1521–1528.

[23] A. Movaghar, R. Lawson, F.N. Egolfopoulos, Radiation effects in confined spherically expanding flames: Application to C_5–C_{10} flames at engine-relevant conditions, Proc. Combust. Inst. 38 (2) (2021) 2195–2203.

[24] F. Halter, G. Dayma, Z. Serinyel, P. Dagaut, C. Chauveau, Laminar flame speed determination at high pressure and temperature conditions for kinetic schemes assessment, Proc. Combust. Inst. 38 (2) (2021) 2449–2457.

[25] A. Mouze-Mornettas, M.M. Benito, G. Dayma, C. Chauveau, B. Cuenot, F. Halter, Laminar flame speed evaluation for CH_4/O_2 mixtures at high pressure and temperature for rocket engine applications, Proc. Combust. Inst. (2022).

[26] C. Bariki, R. Hesse, F. Halter, H. Pitsch, J. Beeckmann, Combined isochoric and isobaric acquisition methodology for accurate flame speed measurements from ambient to high pressures and temperatures, Proc. Combust. Inst. 38 (2) (2021) 2185–2193.

[27] R. Hesse, C. Bariki, M.J. Hegetschweiler, G.T. Linteris, H. Pitsch, J. Beeckmann, Elucidating the challenges in extracting ultra-slow flame speeds in a closed vessel—A CH_2F_2 microgravity case study using optical and pressure-rise data, Proc. Combust. Inst. (2022).

[28] N. Hinton, R. Stone, R. Cracknell, Laminar burning velocity measurements in constant volume vessels–reconciliation of flame front imaging and pressure rise methods, Fuel 211 (2018) 446–457.

[29] J. Beeckmann, L. Cai, H. Pitsch, Experimental investigation of the laminar burning velocities of methanol, ethanol, n-propanol, and n-butanol at high pressure, Fuel 117 (2014) 340–350.

[30] Y. Wu, S. Panigrahy, A.B. Sahu, C. Bariki, J. Beeckmann, J. Liang, A.A. Mohamed, S. Dong, C. Tang, H. Pitsch, Z. Huang, H.J. Curran, Understanding the antagonistic effect of methanol as a component in surrogate fuel models: A case study of methanol/n-heptane mixtures, Combust. Flame 226 (2021) 229–242.

[31] C. Bariki, F. Halter, R. Hesse, C. Chauveau, H. Pitsch, J. Beeckmann, Experimental measurements of laminar flame speeds for highly N_2-diluted ethanol flames under microgravity conditions, Proc. Combust. Inst. (2022).

[32] H. Pitsch, FlameMaster: A C++ computer program for 0D combustion and 1D laminar flame calculations, 1998, URL https://www.itv.rwth-aachen.de/downloads/flamemaster/.

[33] R. Langer, Q. Mao, H. Pitsch, A detailed kinetic model for aromatics formation from small hydrocarbon and gasoline surrogate fuel combustion, Combust. Flame (2022).

[34] S. Dong, S.W. Wagnon, L. Pratali Maffei, G. Kukkadapu, A. Nobili, Q. Mao, M. Pelucchi, L. Cai, K. Zhang, M. Raju, T. Chatterjee, W.J. Pitz, T. Faravelli, H. Pitsch, P.K. Senecal, H.J. Curran, A new detailed kinetic model for surrogate fuels: C3MechV3.3, Appl. Energy Combust. Sci. 9 (2022) 100043.

[35] M. Matalon, B.J. Matkowsky, Flames as gas dynamic discontinuities, J. Fluid Mech. 124 (1982) 239–259.

[36] A.P. Kelley, J.K. Bechtold, C.K. Law, Premixed flame propagation in a confining vessel with weak pressure rise, J. Fluid Mech. 691 (2012) 26–51.

[37] E.F. Fiock, C.F. Marvin, The measurement of flame speeds, Chem. Rev. 21 (3) (1937) 367–387.

[38] M.J. Hegetschweiler, G.T. Linteris, Data reduction tool for spherical constant volume flame experiments, NIST Tech. Note 2148 (2021).

[39] M. Metghalchi, J.C. Keck, Laminar burning velocity of propane-air mixtures at high temperature and pressure, Combust. Flame 38 (1980) 143–154.

[40] M. Elia, M. Ulinski, M. Metghalchi, Laminar burning velocity of methane–air–diluent mixtures, J. Eng. Gas Turbines Power 123 (1) (2001) 190–196.

[41] H. Yu, W. Han, J. Santner, X. Gou, C.H. Sohn, Y. Ju, Z. Chen, Radiation-induced uncertainty in laminar flame speed measured from propagating spherical flames, Combust. Flame 161 (11) (2014) 2815–2824.

[42] A. Omari, L. Tartakovsky, Measurement of the laminar burning velocity using the confined and unconfined spherical flame methods–A comparative analysis, Combust. Flame 168 (2016) 127–137.

[43] Y. Wang, J. Jayachandran, Z. Chen, Effects of pressure rise rate on laminar flame speed under normal and engine-relevant conditions, Combust. Theory Model. 24 (5) (2020) 953–964.

[44] J. Jayachandran, F.N. Egolfopoulos, Effect of unsteady pressure rise on flame propagation and near-cold-wall ignition, Proc. Combust. Inst. 37 (2) (2019) 1639–1646.

[45] R. Lawson, V. Gururajan, A. Movaghar, F.N. Egolfopoulos, Autoignition of reacting mixtures at engine-relevant conditions using confined spherically expanding flames, Proc. Combust. Inst. 38 (2) (2021) 2285–2293.